ACCSCIENCE PUBLISHING

Engineering Science in Additive Manufacturing

ORIGINAL RESEARCH ARTICLE

Effect of build distribution and particle properties on the physical characteristics of laser powder bed fusion of *in situ* alloyed nitinol

Declan Bourke[1,2,3,4]*, Medad C.C. Monu[2,3,4], Paul Healy[1], Alexander Sloane[5], Inam Ul Ahad[2,3,4], and Dermot Brabazon[2,3,4]

[1]Department of Product Development, Fort Wayne Metals Ireland, County Mayo, Connacht, Ireland

[2]I-Form, the SFI Research Centre for Advanced Manufacturing, Dublin City University, Dublin, Ireland

[3]School of Mechanical and Manufacturing Engineering, Faculty of Engineering and Computing, Dublin City University, Dublin, Ireland

[4]DCU Institute for Advanced Processing Technology, Dublin City University, Dublin, Ireland

[5]School of Chemical, Materials and Biological Engineering, Faculty of Engineering, University of Sheffield, Yorkshire, United Kingdom

Abstract

The impact of powder flow characteristics on *in situ* nickel (Ni)-titanium (Ti) alloy formation within the laser powder bed fusion (LPBF) process is poorly understood. In this study, flow segregation patterns of Ni-Ti powder blends within the LPBF build chamber were examined and were found to be influenced by the substrate surface, build layout distribution, and particle size distribution. These segregation patterns significantly impacted relative density (RD) and elasto-caloric properties of *in situ* alloyed nitinol components, with regions of lower RD correlated with lower Ni content and higher phase transformation enthalpies than regions with higher Ni content. It was found that powder segregation rates between Ti and Ni particles were higher for rougher substrates, which also contained higher amounts of unmelted powder than smoother substrates. Furthermore, the position of the unmelted powder relative to the deposition arm sweep impacted powder segregation patterns throughout the build chamber. Powder segregation patterns in the LPBF deposition bed were also affected by differences in material density between Ni and Ti and interparticle cohesive forces. The insights gained from this work provide a route to achieving improved microstructural and chemical homogeneity of *in situ* alloyed nitinol, with tailored thermo-mechanical performance.

Keywords: Nitinol; Additive manufacturing; Laser powder bed fusion; *In situ* alloying

***Corresponding author:**
Declan Bourke
(declan.bourke7@mail.dcu.ie)

Citation: Bourke D, Monu MCC, Healy P, Sloane A, Ahad IU, Brabazon D. Effect of build distribution and particle properties on the physical characteristics of laser powder bed fusion of *in situ* alloyed nitinol. *Eng Sci Add Manuf.* 2025;1(3):025340020. doi: 10.36922/ESAM025340020

Received: August 5, 2025

Revised: August 22, 2025

Accepted: August 28, 2025

Published online: September 18, 2025

1. Introduction

Nitinol is a family of shape memory alloys predominantly composed of nickel (Ni) and titanium (Ti), with properties such as shape memory, super-elasticity, and good fatigue strength and corrosion resistance. It is suited to a wide range of biomedical and industrial applications.[1] However, due to its poor machinability, the range of geometries

that are achievable from conventional manufacturing methods is typically limited to wire, tube, or sheet form.[2] Additive manufacturing offers many advantages over conventional processing, including increased flexibility of design geometry, microstructure, and thermomechanical properties.[3,4] Among the available additive manufacturing technologies, laser powder bed fusion (LPBF) offers high levels of geometrical flexibility, dimensional resolution,[5] microstructural flexibility,[6] chemical purity,[7] and controllable levels of surface roughness.[8] The powder can be pre-alloyed or can be generated by blending powders of the constituent elements and alloying *in situ* during the LPBF process.[9] Challenges with using pre-alloyed powder include time and expense in producing new blends.[10,11] *In situ* alloying offers the opportunity to accelerate the pace of research into complex binary, ternary, and quaternary nitinol alloy systems.[12]

However, *in situ* alloying within additive manufacturing poses numerous challenges compared to pre-alloyed powder. Research to date into *in situ* alloying of nitinol has been limited due to challenges with chemical inhomogeneity,[13] brittle precipitates,[14] and high impurities.[15] Chemical homogeneity can be affected by differences in density and mixing of the elements in the liquid state—leading to higher levels of variation in thermal and mass distribution within the melt pool than pre-alloyed powders[16]—the size of the powder particles relative to the melt pool size,[17] and solute trapping.[18] Chemical homogeneity is also affected by differences in thermal diffusivity and particle size between elemental powders,[10] powder morphology,[19] and unevenness of powder deposition.[20] Furthermore, higher non-uniform thermal distribution in the melt pool leads to a larger surface tension gradient, creating increased Marangoni flow relative to pre-alloyed powders.[21] The exothermic reaction of the mixing enthalpy of Ni and Ti varies with the atomic ratio of the constituent elements[22] and affects underlying thermodynamic conditions, lowering the required input energy.[23] In addition, the highly localized nature of the Ni-Ti exothermic reactions within the rapid cooling environment of LPBF is thought to influence solidification rate and contribute to precipitation of a greater volume of hard, brittle intermetallic phases and higher rates of cracking compared to pre-alloyed material.[16,24]

More than 130 parameters are known to influence the LPBF process,[25] and these can be divided into four broad categories: Laser, scan pattern, temperature profile, and powder parameters.[26] Most studies on *in situ* alloying of nitinol have focused on the impact of factors affecting volume energy density (laser power, scan speed, hatch spacing, and layer thickness) or scan strategies, on microstructural characteristics and thermo-mechanical properties. Stoll *et al.*[15] using equi-atomic elementally blended Ni and Ti, measured significantly higher rates of Ni evaporation compared to pre-alloyed nitinol powder, as well as high levels of cracking and chemical inhomogeneity.[15] Shoji Aota *et al.*[18] found that one of the most important LPBF process parameters for the promotion of increased chemical homogeneity during *in situ* alloying is increased residence time of the laser beam in the molten pool, through the use of slower scan speeds or larger spot size, provided that energy density is kept below the keyholing threshold.[18] Zhao *et al.*,[27] using equi-atomic elementally blended Ni-Ti, recommended scan speeds of <400 mm/s within a laser power range of 100 W–200 W, to maximize chemical homogeneity and relative density (RD).[27] Chmielewska *et al.*[28] achieved success in improving homogeneity and reducing cracking with *in situ* alloying of nitinol using a relatively low volume energy density of 33 J/mm^3, achieved through the use of low laser power (25 W) and moderate scan speed (1000 mm/s), and by employing a remelt scan strategy to reduce thermal gradients and improve melt homogeneity.[28]

None of the previous studies into *in situ* alloying in LPBF examined the impact of powder characteristics such as particle size distribution (PSD) and powder spread ability on nitinol component properties. Recent experimental and discrete element method simulation studies of powder spreading in LPBF systems found that a ratio of layer height to d_{90} <1 led to significantly poorer spread ability than a ratio of layer height to d_{90} > 2.[29,30] Xu & Nan[31] found that spread ability and rate of powder segregation are controlled by not just powder flowability, layer height, and particle size, but also by the shear action of the blade on the powder heap and substrate surface roughness.[31] In particular, flowability is influenced by the granular bond number, which is the ratio of interparticle forces to gravity.[32] For metallic particles within the size range used for LPBF, interparticle forces are dominated by van der Waals forces, and the granular bond number is relatively large.[33] Therefore, it is reasonable to expect powders of blended elements with significant differences in density and cohesiveness, such as Ni and Ti, to be more affected by variations in powder deposition and particle segregation than pre-alloyed powders. It is also reasonable to expect that substrate roughness will impact deposition and segregation patterns in such a blend. Segregation patterns are expected to impact localized chemical concentration ratios, thereby affecting component properties, including phase transformation characteristics.[34] This work aims to study the impact of variations of substrate surface, build layout distribution, and PSD on the resulting homogeneity and properties of components produced from *in situ*

alloyed elementally blended powders within the LPBF process.

2. Data and methods

2.1. Materials

One batch of inert gas atomized spherical Ni powder from AEM, China, with a PSD d_{10}-d_{50}-d_{90} range of 22–33–48 µm, referred to hereafter as Ni(i), was mixed with plasma atomized Ti powder from AP&C, Canada, with a PSD d_{10}-d_{50}-d_{90} range of 21–32–48 µm, referred to hereafter as Ti(i). These were mixed in an acoustic resonance mixer supplied by Resodyn (United States), model LabRam I, at an atomic ratio of Ni = 52%at. and Ti = 48%at., to generate a blend hereafter referred to as $Ni_{(i)}$+$Ti_{(i)}$. A second batch of gas atomized spherical Ni powder from AEM, with a PSD d_{10}-d_{50}-d_{90} range of 33–47–65 µm, referred to hereafter as $Ni_{(ii)}$, was mixed with a second plasma atomized Ti powder from AP&C, with PSD d_{10}-d_{50}-d_{90} range 35–48–64, referred to hereafter as $Ti_{(ii)}$, in the same manner as above, to generate a blend hereinafter referred to as $Ni_{(ii)}$+$Ti_{(ii)}$. PSD was measured on a Malvern Mastersizer 3000 (Malvern Panalytical, United Kingdom) dynamic light scattering unit.

2.2. Cuboidal LPBF sample fabrication

To study the impact of specimen layout and powder bed substrate on powder deposition and segregation, powder batch $Ni_{(i)}$+$Ti_{(i)}$ was used to three-dimensionally print various specimens of size 7 × 7 × 7 mm^3 in an AconityMINI LPBF system with a 200 W fiber laser of 1068 nm wavelength, in three different layouts, A, B and C per Figure 1, each with different proportions of melted versus unmelted substrate. Layout A consisted of six columns of specimens printed in the lower half of the build plate (colored orange), and one central column with specimens printed along the entire sweep of the deposit arm (colored green), with largely unmelted substrate in the upper half of the coater arm sweep. Layout B consisted of six columns of specimens printed in the upper half of the build plate (colored blue) and one central column with specimens printed along the entire sweep of the coater arm (colored green), with largely unmelted powder in the lower half of the coater arm sweep. Layout C consisted of seven columns with specimens printed along most of the coater arm sweep (colored green).

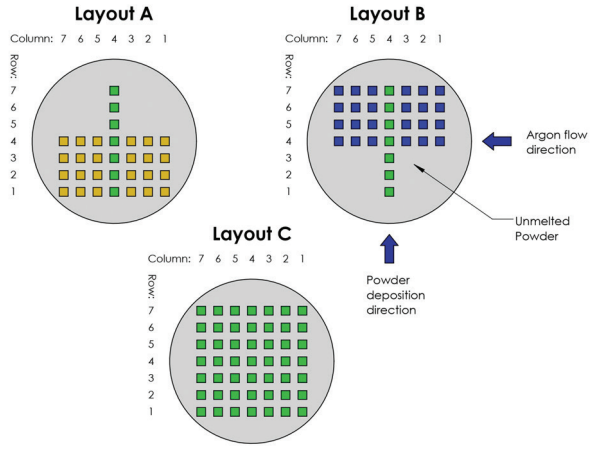

Figure 1. Schematic of build layouts A, B, and C

Process settings used for all specimens were laser power 200 W, scan speed 800 mm/s, hatch spacing 150 µm, layer thickness 60 µm, and spot size 111 µm. The laser scan direction was rotated by 70° after completion of each layer. The re-coater arm deposition speed over the LPBF powder bed was fixed for all trials at 50 mm/s.

2.3. Powder fluidity assessment

To study the impact of PSD on powder deposition and segregation, powder batch $Ni_{(ii)}$+$Ti_{(ii)}$ PSD d_{50} = 44 µm, was used to three-dimensionally print specimens of the same size (7 × 7 × 7 mm^3) using the same settings as described above, in accordance with Layout A (Figure 1) for comparison with powder batch $Ni_{(i)}$+$Ti_{(i)}$ PSD d_{50} = 32 µm. Properties relating to flow energy and bulk density were measured for each batch of powder before and after blending with a Freeman Technology (United Kingdom) Model FT4 Powder Rheometer®.[35] Each measurement on the FT4 device was performed on virgin powder conditioned immediately before testing to remove any variability that may have been introduced while loading the powder by passing a rotating blade at low energy through the powder column, minimizing any precompaction or excess air effects. The flow energy properties measured were basic flow energy (BFE), which is the energy required to establish a particular flow pattern in a conditioned, precise volume of powder, under compression, and specific energy (SE), which is a measure of how powder will flow in an unconfined or low stress environment for a conditioned, precise volume of powder. The conditioned bulk density, the density of a 25 mL powder volume conditioned on the FT4 in the manner described above, was also measured before weighing.

Powder dynamic flow and particle cohesiveness were measured using a GranuDrum powder fluidity measurement instrument from GranuTools™ (Belgium) for the Ni, Ti, and blended Ni-Ti powders from batch $Ni_{(ii)}$+$Ti_{(ii)}$.[36] This automated powder flowability device uses a horizontal cylinder with transparent side walls, which contains a powder volume and rotates around its axis at incremental angular velocities. A high-frequency

optical camera (Granutools, Belgium) was used to capture images of the edge of the powder profile for each angular velocity. The dynamic angle of repose was computed from the average edge profile position. This is a measure of flowability that depends on both contact friction forces and interparticle cohesive forces, and decreases with improved flowability.[37] Fluctuations in the edge profile were monitored to calculate the cohesive index (CI), a measure of inter-particle cohesion and flowability influenced by a combination of Van der Waals, capillary, and electrostatic interactions. Based on N = 50 images, the standard deviation (σ_x) of the fluctuation height of the interface was calculated using Equation I[37]:

$$\sigma_x = \sqrt{\frac{\Sigma_{i=1}^{\mathbb{N}y(x)} \left(\bar{y}(x) - y_i(x)\right)^2}{\mathbb{N}_y(x)}} \quad \text{(I)}$$

where $\bar{y}(x)$ is the mean coordinate height for the slope of the angle of repose at position x, and y_i (x) is the measured coordinate height at position x. CI was then calculated by averaging σ_x over the visible length of the interface. The drum rotation speed was mapped to the equivalent recoater deposition arm speeds by calculating the tangential velocity and multiplying the rotational speed (radians/second) by the drum radius (r = 42 mm).[38] By this calculation, the recoater arm speed employed in the LPBF trials, 50 mm/s, corresponded to a rotating drum speed of 11.4 rpm. Drum rotating speeds tested ranged from 2 rpm to 60 rpm.

2.4. Specimen characterization

RD measurements were performed on all specimens using Archimedes' principle in accordance with ASTM B962-17, using a Sartorius (Germany) weighing scale with measurement accuracy ± 0.1 mg and acetone, against a theoretical maximum density of 6.55 g/cm^3.

Differential scanning calorimetry (DSC) testing on selected specimens was performed in accordance with ASTM F2004-17 on a TA Instruments (United States) Discovery DSC2500 device, subjected to a temperature range of −150°C–+150°C in a nitrogen atmosphere at heating and cooling rates of 10°C/min.

Sample preparation for optical, energy-dispersive X-ray spectroscopy (EDX), and X-ray diffraction (XRD) analysis was performed by grinding cold resin mounts with silicon carbide papers of 80, 300, 600, 800, and 1,200 grit, and polishing with diamond suspension of 9, 3, and 1 µm at a rotary speed of 200–250 rpm. For optical analysis, 10 mL of nitric acid, 4 mL of hydrofluoric acid, and 40 mL of deionized water were utilized as an etchant after polishing. EDX measurements were performed on a Zeiss (Germany) EVO LS-15 scanning electron microscope (SEM) and analyzed with Oxford Instruments® Aztec software (version 6.2). Ni content was measured by the map spectrum over an area 1.8 × 2.2 mm^2 (magnification 150×) near the center of vertical sections of selected specimens. Statistical analysis of RD, DSC, and XRD data was performed using Microsoft Excel (version 2506) and Minitab (version 22.1).

Micro-computed tomography (CT) for porosity measurement was performed using a GE Phoenix V|tome|x (Waygate Technologies, Germany) device on a central section measuring 2 × 2 × 2 mm^3 of six selected specimens representing low, nominal, and high RD. Measurement resolution was 10 µm, and 600 images were taken per scan.

XRD measurements were performed on an Anton Paar (Austria) XRDynamic 500 for phase identification between 2Θ 35° and 80°, using a copper K-alpha X-ray source with a wavelength of 1.5406 Å. Specimens were sectioned parallel to the build direction (vertical plane), and ground and polished, such as the SEM-EDX specimens. Relevant NiTi crystal structures from the Crystallography Open Database[39] were used for indexing the XRD spectra. Quantitative spectral analysis of phases and their volume fractions was achieved by Rietveld refinement using the FullProf software (version April 2024),[40] integrated into the Match! software (version 4.1).[41] From this data, the percentage phase composition was calculated.

3. Results

3.1. Powder characterization

Scanning electron microscopy micrographs for each of the powder batches are presented in Figure 2, demonstrating good sphericity for all powders, both before and after mixing. PSD results for the powder batches are presented in Figure 3, confirming closely matched powder PSDs for Ni and Ti in each batch. The d_{10}-d_{50}-d_{90} for Ni and Ti for $Ni_{(i)}$+$Ti_{(i)}$ and $Ni_{(ii)}$+$Ti_{(ii)}$ measured 21–32–49 µm and 33–47–65 µm, respectively.

Powder flow fluidity and bulk density (FT4) as well as dynamic flow and cohesive measurements (Granudrum) are presented in Figures 4 and 5, respectively. BFE, measured using the FT4, for batch $Ni_{(i)}$+$Ti_{(i)}$ was 656 mJ compared to 595 mJ for batch $Ni_{(ii)}$+$Ti_{(ii)}$. Similarly, SE was higher for batch $Ni_{(i)}$+$Ti_{(i)}$ at 3.28 mJ/g compared to 2.58 mJ/g for $Ni_{(ii)}$+$Ti_{(ii)}$. Within each batch, the FT4 basic flow energy for the Ni powder, which averaged 972 mJ across both batches, was significantly higher than for the Ti powder, which averaged 398 mJ across both batches. The conditioned bulk density of batch $Ni_{(i)}$+$Ti_{(i)}$ at 3.75 g/mL was marginally lower than for batch $Ni_{(ii)}$+$Ti_{(ii)}$ at 3.88 g/mL.

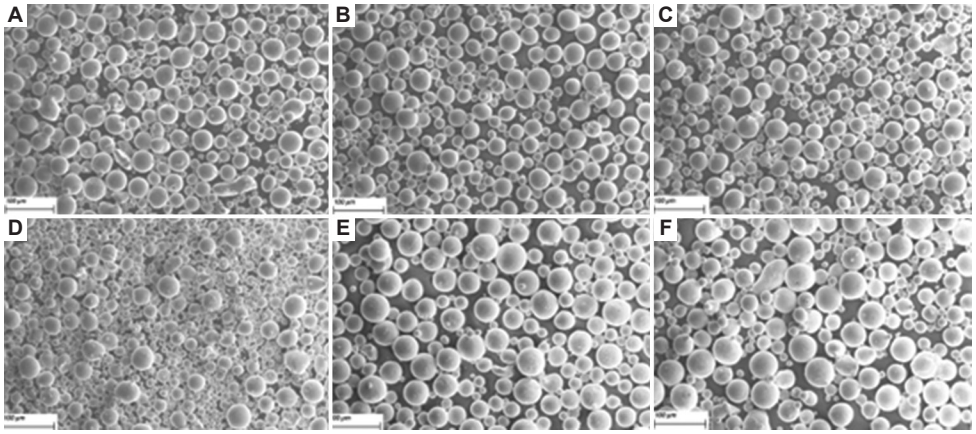

Figure 2. Scanning electron microscopy micrographs of the powders. (A) $Ni_{(i)}$, (B) $Ti_{(i)}$, (C) $Ni_{(i)}$+$Ti_{(i)}$, (D) $Ni_{(ii)}$, (E) $Ti_{(ii)}$, and (F) $Ni_{(ii)}$+$Ti_{(ii)}$. Scale bar: 100 μm; magnification: 500×.
Abbreviations: Ni: Nickel; Ti: Titanium.

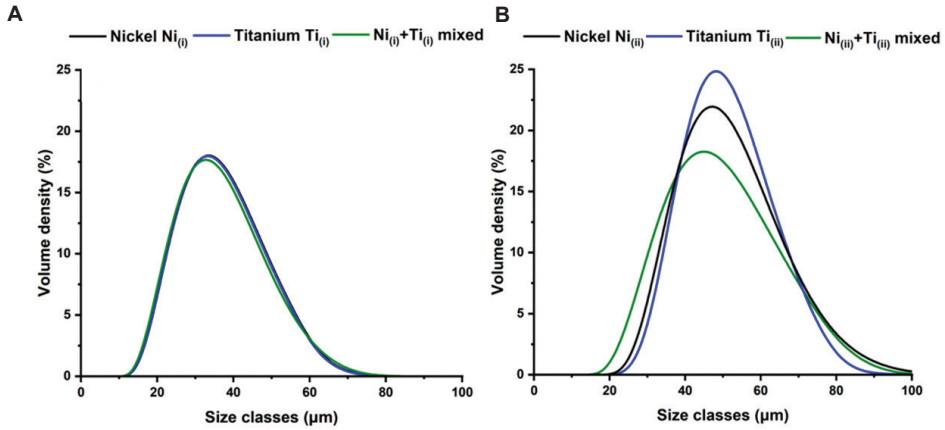

Figure 3. Particle size distributions of the powders used in this study. *In situ* elementally blended (A) $Ni_{(i)}$+$Ti_{(i)}$ and (B) $Ni_{(ii)}$+$Ti_{(ii)}$.

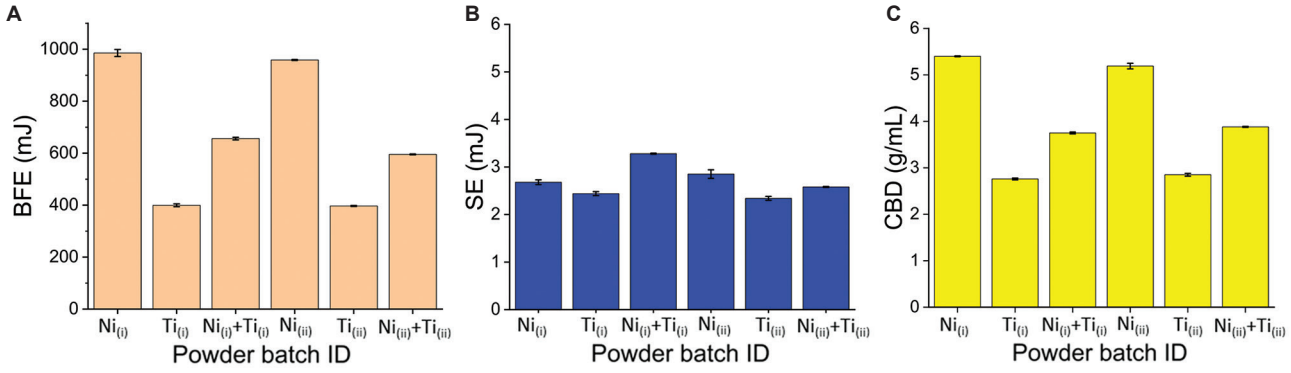

Figure 4. Powder FT4 fluidity characterization results. (A) Basic flow energy (BFE), (B) specific energy (SE), and (C) conditioned bulk density (CBD).
Abbreviations: Ni: Nickel; Ti: Titanium.

The BFE and SE measurements for the Ni powders were significantly lower than those of their corresponding Ti powders of the same nominal size range.

The dynamic angle of repose on the Granudrum device was similar for both the Ni and Ti powders across the full range of speeds tested (Figure 5B). The measured

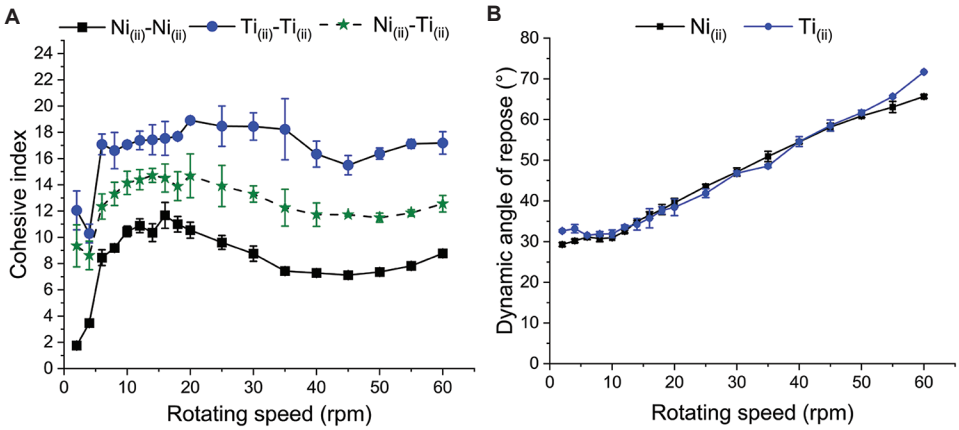

Figure 5. Powder granudrum dynamic flow results for $Ni_{(ii)}$-$Ni_{(ii)}$, $Ti_{(ii)}$-$Ti_{(ii)}$, and $Ni_{(ii)}$+$Ti_{(ii)}$. (A) Cohesive index and (B) dynamic angle of repose.
Abbreviations: Ni: Nickel; Ti: Titanium.

CI as a function of rotating speed, for Ni-Ni, Ti-Ti, and Ni-Ti particle interactions, is presented in Figure 5A. At all rotating drum speeds, the CI for Ti-Ti interactions was significantly higher than that of the Ni-Ni interactions. At a rotating drum speed of 11.4 rpm, which corresponds most closely to the deposition arm speed of 50 mm/s as discussed earlier, the CI for the Ti-Ti powder particle interaction was 1.62 times higher than the Ni-Ni powder particle interaction, indicating significantly higher interparticle cohesive forces for the Ti than for the Ni powder. The CI recorded for the blended Ni-Ti batch was close to the average of the Ni-Ni and Ti-Ti measurements.

3.2. RD

Average RD was measured, and standard deviation was calculated for each of the four trials (Figure 6), for each column (Figure S1), and for each row (Figures 7 and S2).

Average RD for the three trials with batch $Ni_{(i)}$+$Ti_{(i)}$ (PSD d_{50} = 32 μm) did not vary significantly from each other, measuring 98.6%, and ranging from 97.7% to 99.4% across the three runs (Figure 6). Standard deviation of RD for each of these three trials was 0.39% for Layout A, 0.44% for Layout B, and 0.26% for Layout C.

Average RD for the trial from batch $Ni_{(ii)}$+$Ti_{(ii)}$, (PSD d_{50} = 44 μm), was significantly different from batch $Ni_{(i)}$+$Ti_{(i)}$, and measured 97.1%, ranging from 96.2% to 98.5%. The standard deviation for this trial was the highest of all the trials at 0.59%.

An analysis of RD trends by column position (Figure S1) revealed no correlation with RD. Standard deviation across the seven columns for each trial averaged 0.41% for batch $Ni_{(i)}$+$Ti_{(i)}$ Layout A, 0.44% for batch $Ni_{(i)}$+$Ti_{(i)}$ Layout B, 0.27% for batch $Ni_{(i)}$+$Ti_{(i)}$ Layout C, and 0.62% for batch $Ni_{(ii)}$+$Ti_{(ii)}$ Layout A

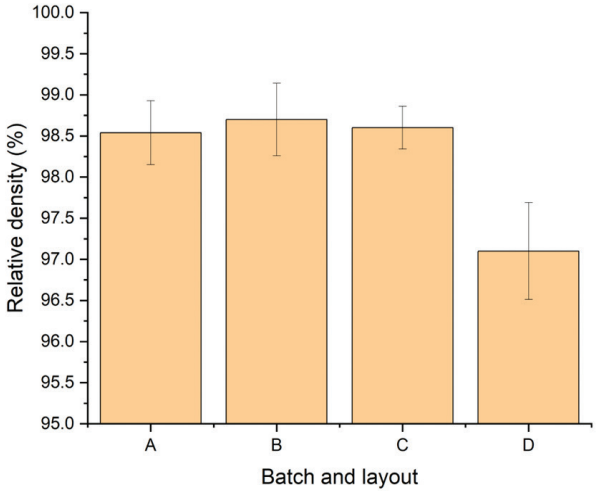

Figure 6. Average relative density for each run. (A) batch $Ni_{(i)}$+$Ti_{(i)}$ layout A, (B) batch $Ni_{(i)}$+$Ti_{(i)}$ layout B, (C) batch $Ni_{(i)}$+$Ti_{(i)}$ layout C, and (D) batch $Ni_{(ii)}$+$Ti_{(ii)}$ layout A.
Abbreviations: Ni: Nickel; Ti: Titanium.

An analysis of RD trends by row position (Figures 7 and S2) revealed a consistent correlation between RD and row position within each layout. With reference to Figure 1, this indicates that the build position concerning powder deposition distance has significantly impacted RD. Standard deviation by row for each trial averaged 0.19% for batch $Ni_{(i)}$+$Ti_{(i)}$ Layout A, 0.29% for batch $Ni_{(i)}$+$Ti_{(i)}$ Layout B, 0.15% for batch $Ni_{(i)}$+$Ti_{(i)}$ Layout C, and 0.22% for batch $Ni_{(ii)}$+$Ti_{(ii)}$ Layout A.

RD variation was observed to be influenced by the powder bed substrate, showing distinct RD patterns: Regions where the deposition arm had travelled over

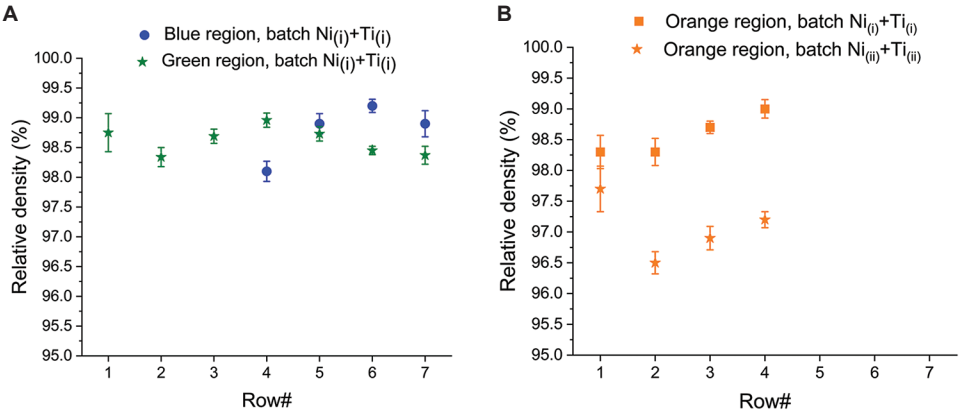

Figure 7. Relative density by row. (A) blue and green regions, batch $Ni_{(i)}$+$Ti_{(i),}$ layouts B. (B) Orange regions, batches $Ni_{(i)}$+$Ti_{(i)}$ and $Ni_{(ii)}$+$Ti_{(ii)}$, layout A. Abbreviations: Ni: Nickel; Ti: Titanium.

predominantly printed specimens (orange and green regions, Figure 1) differed from those where it traveled over mostly unmelted powder before reaching the specimens (blue region, Figure 1). Figure 7A compares the RD pattern of the blue and green regions for batch $Ni_{(i)}$+$Ti_{(i)}$ and demonstrated that by the time the powder is deposited at Row 4, a significant difference has emerged in the RD of the two regions, with Row 4 of the green region having an average RD of 99.0% (σ = 0.11%) and Row 4 of the blue region having an average RD of 98.2% (σ = 0.36%). Furthermore, RD for the green and blue regions exhibited opposite trends between Rows 4 and 7: in the green region, RD at Row 6 decreased to 98.4% (σ = 0.10%), whereas in the blue region, RD at Row 6 increased to 99.2% (σ = 0.11%).

RD variation was also observed to be influenced by average particle size. Figure 7B reveals a significant difference in the RD distributions of the orange region for batch $Ni_{(i)}$+$Ti_{(i)}$ compared to the orange region for batch $Ni_{(ii)}$+$Ti_{(ii)}$. Specifically, RD in Row 1 was lower for $Ni_{(ii)}$+$Ti_{(ii)}$ than for $Ni_{(i)}$+$Ti_{(i)}$. $Ni_{(ii)}$+$Ti_{(ii)}$ also exhibited a significantly wider range of RD variation than $Ni_{(i)}$+$Ti_{(i).}$ This is most notable between Row 1 and Row 2, where RD is unchanged at 98.2% (σ = 0.33% and σ = 0.20% for Row 1 and 2, respectively), whereas RD for $Ni_{(ii)}$+$Ti_{(ii)}$ decreased from 97.5% (σ = 0.37%) to 96.5% (σ = 0.18%). Both batches showed an increasing trend in RD between Rows 2 and 4, with RD = 99.0% (σ = 0.13%) at Row 4 for batch $Ni_{(i)}$+$Ti_{(i)}$, and RD = 97.2% (σ = 0.13%) at Row 4 for batch $Ni_{(ii)}$+$Ti_{(ii)}$.

3.3. Chemistry

Ni composition measurements, based on EDX map spectra as described above, on 50 selected specimens divided equally between both powder batches, averaged 49.4%at., varying from 47.7%at. to 51.6%at. A regression analysis of RD against Ni content for these specimens is presented in Figure 8,

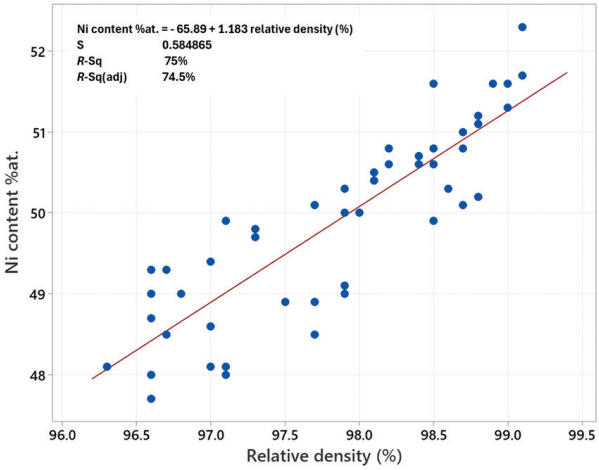

Figure 8. Correlation between nickel content and relative density for *in situ* alloyed specimens, combining batches $Ni_{(i)}$+$Ti_{(i)}$ and $Ni_{(ii)}$+$Ti_{(ii)}$ Abbreviations: Ni: Nickel; *R*-sq: *R*-squared; Ti: Titanium.

demonstrating a strong positive correlation with a Pearson coefficient of $R = 0.87$ and an R^2 coefficient of 74.5%.

3.4. Micro-CT analysis

Density based on porosity measurements from micro-CT scans for the six selected specimens ranged from 99.31% to 99.97%. As stated earlier, these specimens represented the lowest, highest, and nominal RD, as measured by the Archimedes method. Figure S3 shows the micro-CT density results plotted as a function of Archimedes' RD and demonstrates no correlation between the two attributes. This indicates that the variation in RD across the specimens is primarily driven by Ni content and not porosity.

3.5. Phase transformation

Phase transformation temperatures, hysteresis values, ranges, and enthalpies are summarized in Table 1 and

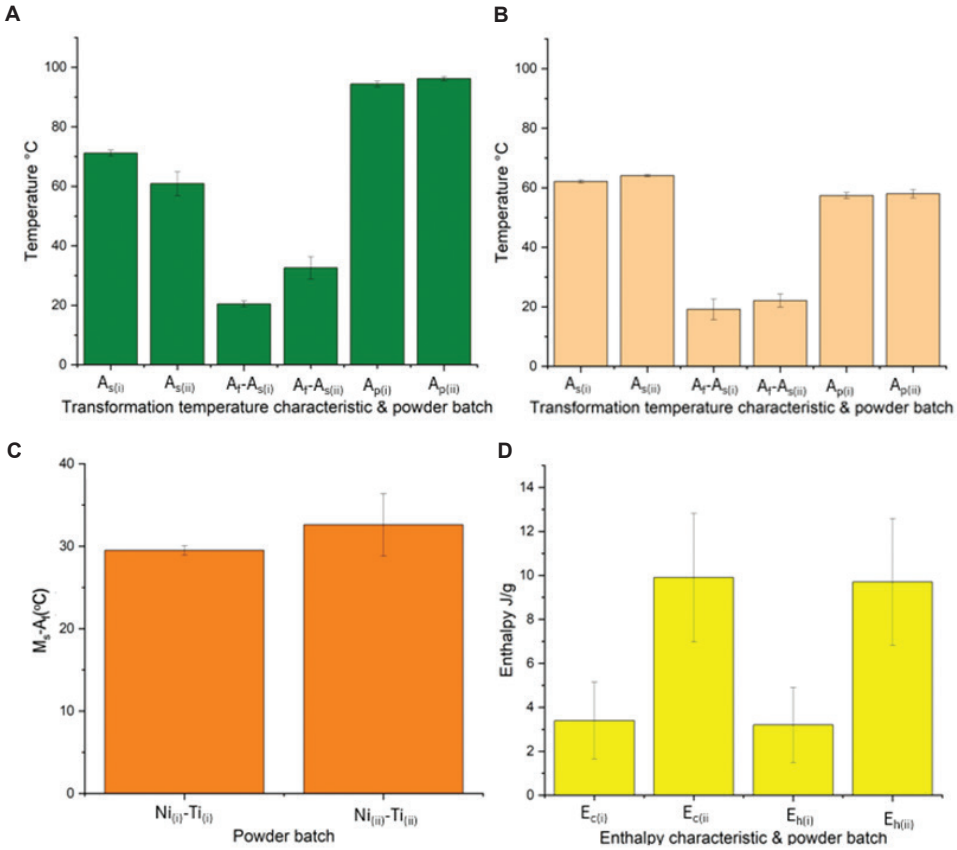

Figure 9. Phase transformation characteristics for powder batches $Ni_{(i)}+Ti_{(i)}$ and $Ni_{(ii)}+Ti_{(ii)}$. (A) Heating cycle transformation temperatures and ranges, (B) cooling cycle transformation temperatures and ranges, (C) hysteresis values, and (D) enthalpies.
Abbreviations: A_f: Austenitic finish temperature; A_p: Austenitic peak temperature; A_s: Austenitic start temperature; E_c: Cooling cycle (exothermic) phase transformation enthalpy; E_h: Heating cycle (endothermic) phase transformation enthalpy; M_f: Martensitic finish temperature; M_p: Martensitic peak temperature; M_s: Martensitic start temperature; Ni: Nickel; Ti: Titanium.

Table 1. Differential scanning calorimetry data for the elementally mixed powders for the low and high particle size distributions

Temperature	Batch	M_s	M_s–M_f	M_p	A_s	A_f–A_s	A_p	A_f–M_s	E_c (J/g)	E_h (J/g)
Average (°C)	$Ni_{(i)}+Ti_{(i)}$	62.1	19.2	57.4	71.2	20.5	84.4	29.5	3.4	3.2
	$Ni_{(ii)}+Ti_{(ii)}$	64.1	22.1	58.0	60.9	32.6	86.2	32.6	9.9	9.7
Minimum (°C)	$Ni_{(i)}+Ti_{(i)}$	60.2	13.5	53.8	68.7	18.4	82.0	28.3	1.4	1.3
	$Ni_{(ii)}+Ti_{(ii)}$	63.3	18.2	54.0	54.2	24.3	84.7	24.3	5.1	5.0
Maximum (°C)	$Ni_{(i)}+Ti_{(i)}$	63.5	28.5	58.7	73.4	22.5	85.9	30.8	8.7	8.4
	$Ni_{(ii)}+Ti_{(ii)}$	64.9	25.9	60.4	70.0	38.8	87.6	38.8	15.5	14.9

Abbreviations: A_f: Austenitic finish temperature; A_p: Austenitic peak temperature; A_s: Austenitic start temperature; E_c: Cooling cycle (exothermic) phase transformation enthalpy; E_h: Heating cycle (endothermic) phase transformation enthalpy; M_f: Martensitic finish temperature; M_p: Martensitic peak temperature; M_s: Martensitic start temperature; Ni: Nickel; Ti: Titanium.

illustrated in Figure 9. Martensitic start, martensitic peak, martensitic finish, austenitic start, austenitic peak, and austenitic finish temperatures are represented by M_s, M_p, M_f, A_s, A_p, and A_f, respectively. Cooling cycle (exothermic) and heating cycle (endothermic) phase transformation enthalpies are represented by E_c and E_h, respectively. M_s and M_p did not vary significantly, with M_s measuring an average of 62.1°C with a min-max range of 60.2°C–63.5°C for $Ni_{(i)}+Ti_{(i)}$, and an average of 64.1°C with a min-max range of 63.3°C–64.9°C for $Ni_{(ii)}+Ti_{(ii)}$ The widths of the martensitic transformation curves (M_s–M_f) were 19.2°C for $Ni_{(i)}+Ti_{(i)}$ and 22.1°C for $Ni_{(ii)}+Tii_{(i)}$. The widths of the austenitic transformation curves (A_s–Af) were 20.5°C for $Ni_{(i)}+Ti_{(i)}$ and 32.6°C for $Ni_{(ii)}+Tii_{(i)}$. There was a significant

difference in average A_s and standard deviation between the two batches, with average A_s = 71.2°C (σ = 0.98) for $Ni_{(i)}$+$Ti_{(i)}$ and 60.9°C (σ = 4.02) for $Ni_{(ii)}$+$Ti_{(ii)}$. A_p did not vary significantly across all specimens for both batches, from a minimum temperature of 82.0°C to a maximum temperature of 87.6°C.

Figure 10 shows the DSC transformation curves for selected specimens, representative of the median enthalpy for each batch. All specimens exhibited direct phase transformations on heating (M–A) and cooling (A–M) cycles, with no evidence of secondary R-phase. As shown in Table 1, average cooling and heating enthalpy values for batch $Ni_{(i)}$+$Ti_{(i)}$ were 3.4 J/g and 3.2 J/g, respectively, considerably lower than the corresponding values for batch $Ni_{(ii)}$+$Ti_{(ii)}$ at 9.9 J/g and 9.7 J/g. There was considerable variation in phase transformation enthalpy within each batch, with cooling enthalpy for $Ni_{(i)}$+$Ti_{(i)}$ ranging from a minimum of 1.4 J/g to a maximum of 8.7 J/g. For batch $Ni_{(ii)}$+$Ti_{(ii)}$, cooling enthalpy varied from a minimum of 5.1 J/g to a maximum of 15.5 J/g. In general, transition enthalpy changes were 1%–5% higher in the cooling cycle than in the heating cycle. The enthalpy values were influenced by specimen position and were strongly negatively correlated with RD. The regression plot in Figure 11 has an R^2 coefficient of 88%.

3.6. XRD phase analysis

Analysis of XRD results using Rietveld refinement across 13 specimens, selected for high, low, and nominal phase transformation enthalpy across both batches, indicated that at room temperature, more than 95% of the area fraction in all specimens consisted of a mixture of two phases, austenite B2 and martensite B19'. Figure 12 shows representative XRD plots for low, nominal, and high enthalpy. The area fraction of B19' varied from 9% to 63% and was positively correlated with phase transformation enthalpy, as shown in Figure 13.

3.7. Microstructure

A multi-modal grain structure was observed in all specimens, as demonstrated in Figure 14. This consisted of near-equiatomic (Ni = 48%at. to 52%at.) coarse columnar grains, approximately 50 µm–150 µm in size, interspersed with clusters of Ni-poor (Ni = 45%at. to 48%at.) equi-axed grains <2 µm in size and Ni-poor dendritic grains up to 5 µm in length. Regions of unmelted or partially melted Ti (Ni < 10%at.) and coarse Ti_2Ni precipitates (Ni = 33.3%) up to 30 µm in size were also present.

4. Discussion

4.1. RD

The positive correlation between Ni content and RD (Figure 8) and the absence of any correlation between density measured by micro-CT porosity and RD, as measured by Archimedes (Figure S3), indicate that the patterns in RD in Figure 7 are primarily attributable to chemistry variation. Chemistry variation may be due to one or both of two factors: Variation in particle size throughout the powder bed, which impacts chemical homogeneity, and melt pool size and temperature, causing variations in the rate of Ni evaporation,[42] or segregation of the Ni and Ti particles during deposition on the powder bed. The repeating trends in RD for each row in all four trials (Figure S2), in the direction of powder deposition, and the absence of any corresponding trend by column (Figure S1), indicate that RD variation is attributable to powder deposition patterns as a function of distance from the start position of the spreader arm.

Regarding Figure 7, the segregation patterns by row number, as defined in Figure 1, follow consistent non-linear patterns. For powders melted in Rows 1–4 (green and orange regions), there was a decrease in RD followed by an increase between Rows 2 and 4, and a decrease between Rows 4 and

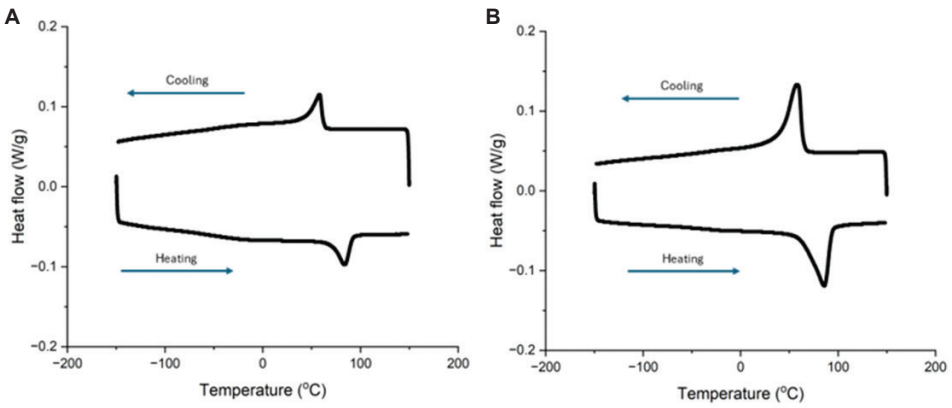

Figure 10. Differential scanning calorimetry curve for selected median specimens. *In situ* batch (A) $Ni_{(i)}$+$Ti_{(i)}$, and (B) $Ni_{(ii)}$+$Ti_{(ii)}$. Abbreviations: Ni: Nickel; Ti: Titanium.

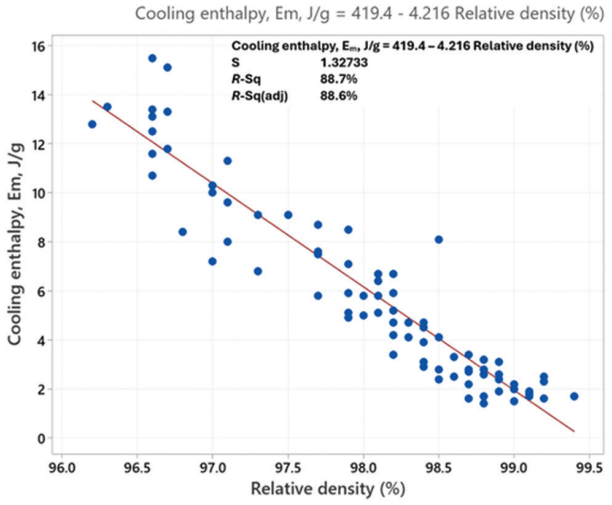

Figure 11. Phase transformation cooling enthalpy versus relative density, combining batches $Ni_{(i)}$+$Ti_{(i)}$ and $Ni_{(ii)}$+$Ti_{(ii)}$.
Abbreviations: Ni: Nickel; *R*-sq: *R*-squared; Ti: Titanium.

7. For unmelted powders in Rows 1–3 (blue region), there was an increase in RD from Rows 4 to 6, followed by a slight decrease between Rows 6 and 7. This indicates that the substrate over which the powder travels (melted versus unmelted regions) impacts deposition patterns.

The effect of the substrate on powder deposition patterns can also be assessed by comparing the standard deviation in RD across the layouts. Batch $Ni_{(i)}$+$Ti_{(i)}$ Layout C had the lowest standard deviation of the four trials, indicating that the rate of segregation between Ti and Ni over powder bed regions with the highest fraction of melted powder and smoothest substrate is lower than for regions containing higher fractions of unmelted powder. This may be attributable to lower friction resistance against the movement of the powder arm over smoother areas with higher fractions of melted powder.

Powder flow in LPBF is controlled by competing factors, including a cohesive effect due to interparticle forces and a geometric effect due to spreader arm clearance with the powder particles.[32] It is known that for particles below 100 µm in size, the ratio of interparticle forces to gravity, known as the Granular Bond number, B_0, is negatively correlated with flowability,[43] and can be expressed as Equation II[33]:

$$B_0 = \frac{F_C}{Fw} \quad \text{(II)}$$

where F_C is the inter-particle cohesive force and F_W is the gravimetric force. F_C is directly proportional to the CI for each bulk powder interaction.[36] Furthermore, because the PSDs of the batches of Ti and Ni powders are closely matched for each blend (Figure 3), F_W is directly proportional to the density of each material. The ratio between the bond numbers B_{oTi} and B_{oNi} for the Ti-Ti and Ni-Ni powder interactions, respectively, can therefore be expressed as Equation III:

$$\frac{B_0 T_i}{B_{oN_i}} = \frac{CI_{T_i} \cdot \rho_{N_i}}{CI_{N_i} \cdot \rho_{T_i}} \quad \text{(III)}$$

The dynamic flow results from the GranuDrum trials (Figure 5A) demonstrated that the ratio of the interparticle cohesive forces, CI_{Ti}: CI_{Ni}, at rotating speed corresponding to the deposition speed in the trials (11 rpm/50 fpm) is 1.63. The gravimetric force ratio ρ_{Ni}: ρ_{Ti} = 8.89: 4.51 = 1.97.[44,45] Multiplying the CI_{Ti}: CI_{Ni} by the gravimetric force ratio ρ_{Ni}:ρ_{Ti} gives 3.2, meaning the Bond number of the Ti-Ti powder interaction is 3.2 times higher than that of the Ni-Ni powder interaction, and the two materials are likely to spread at different rates and segregate within the powder bed. The dynamic flow CI results for the Ni-Ti blend indicate that the Ni-Ti interparticle cohesion is an average of the Ni-Ni and Ti-Ti interparticle cohesion.

Powder deposition patterns are also influenced by the PSD range, with smaller particles being deposited closer to the start position of the deposition arm sweep than larger particles, as demonstrated by Mussatto *et al.*[20]

The higher variation in RD and lower overall average RD of $Ni_{(ii)}$+$Ti_{(ii)}$ compared to $Ni_{(i)}$+$Ti_{(i)}$ (Figure 6) can be partly explained by the larger particle size in the former, leading to larger melt pools and longer homogenization times, increasing Ni evaporation[9] and chemical inhomogeneity.[10,46] Another reason for the higher variation in RD within the batch with the larger particle size is the effect of the ratio between layer thickness and d_{90} particle size on flowability.[47] Ahmed *et al.*[30] found that flowability improved as this ratio increased, with optimum flowability occurring at a ratio of 2.5 or greater.[30] The ratio between layer thickness (t = 60 µm) and d_{90} particle size is 0.92 for $Ni_{(ii)}$+$Ti_{(ii)}$ and 1.22 for $Ni_{(i)}$+$Ti_{(i)}$, indicating reduced flowability for the former, which is most likely linked to an increased rate of particle segregation. Another factor that is likely contributing to increased variation in RD $Ni_{(ii)}$+$Ti_{(ii)}$ compared to $Ni_{(i)}$+$Ti_{(i)}$, based on earlier observations of higher powder segregation over substrates of higher roughness, is that the larger powder particles are creating a rougher substrate than the smaller particles.

The higher FT4 BFE and SE for $Ni_{(i)}$+$Ti_{(i)}$ relative to $Ni_{(ii)}$+$Ti_{(ii)}$ (Figure 4A and B) are likely attributable to the wider PSD span and higher fraction of fine powder of the former.[48] Despite the higher flow energy, the lower overall segregation rate within $Ni_{(i)}$+$Ti_{(i)}$ indicates that FT4 bulk

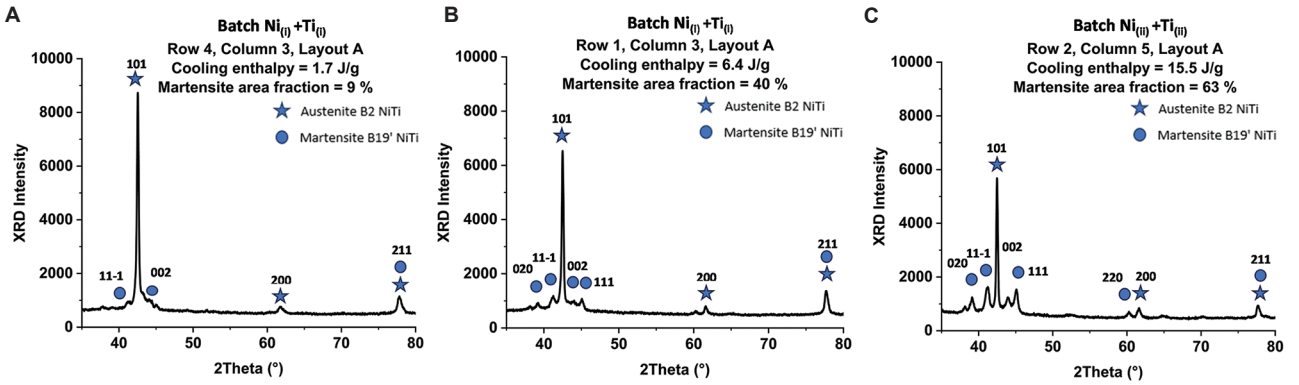

Figure 12. X-ray diffraction plots of selected specimens. (A) Low cooling enthalpy and low martensite area fraction, (B) nominal cooling enthalpy and nominal martensite area fraction, and (C) high cooling enthalpy and high martensite area fraction.
Abbreviations: Ni: Nickel; Ti: Titanium; XRD: X-ray diffraction.

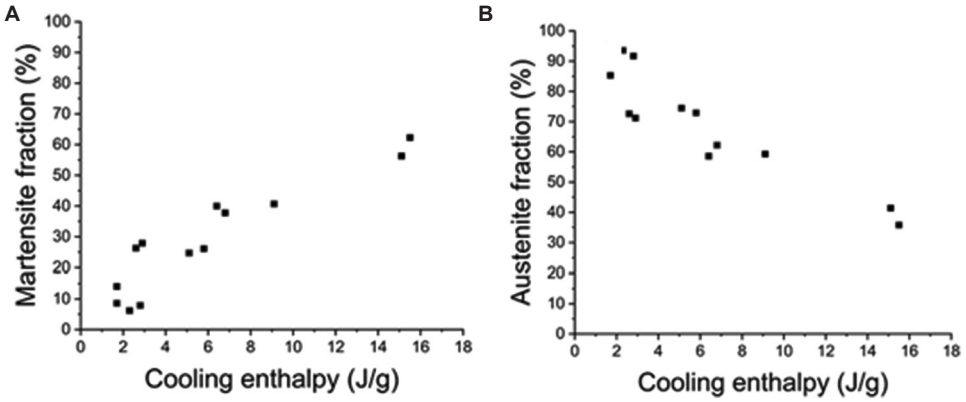

Figure 13. Phase transformation. (A) Cooling enthalpy versus martensite and (B) cooling enthalpy versus austenite area fractions of selected specimens calculated by Rietveld analysis of X-ray diffraction data.

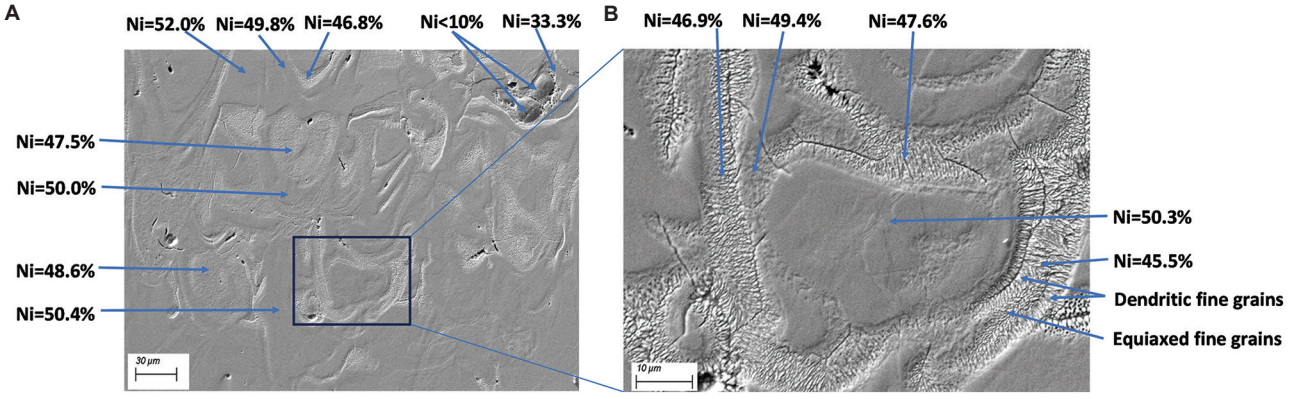

Figure 14. Representative vertical cross-section and energy-dispersive X-ray spectroscopy map spectra results for the vertical cross-section of an *in situ* alloyed specimen. Batch $Ni_{(i)}$+$Ti_{(i)}$ at (A) low magnification (Scale bar: 30 µm; magnification: 1000×) and (B) a higher magnification (Scale bar: 10 µm; magnification: 4000×) of the identified region in (A).
Abbreviations: Ni: Nickel; Ti: Titanium.

flow energy characteristics, as measured, within the ranges tested, have a lesser influence on powder flow segregation than the other factors discussed above. In summary, the segregation patterns of the Ni and Ti powders in the LPBF powder bed are primarily affected by differences in material density, interparticle cohesive forces, the substrate over which the powder travels during deposition, and the PSD.

4.2. Phase transformation behavior

The variation in phase transformation enthalpy as a function of RD/Ni content (Figure 11) is a remarkable feature of the results. Phase transformation enthalpy ΔH_{NET} is made up of chemical, $\Delta H_{CH,}$ elastic, ΔH_{EL}, and surface friction, ΔH_{FR}, components, in accordance with Equation IV.[49]

$$\Delta H_{NET} = \Delta H_{CH} + \Delta H_{EL} + \Delta H_{FR} \quad \text{(IV)}$$

The chemical driving force, ΔH_{CH}, generates reversible transformation energy and depends on the volume fraction of reversible NiTi.[50] XRD analysis (Figure 12) indicated the presence of both B19' martensite phase and B2 austenite phase at room temperature, with varying relative area fractions. The positive correlation between the calculated area fraction of B19' and phase transformation enthalpy in Figure 13 indicates that the B19' area fraction is providing the chemical driving force for phase transformation behavior. The negative correlation between the B2 area fraction and phase transformation enthalpy indicates that the driving force of the B2 microstructure may be more significantly inhibited by localized chemical inhomogeneity than that of the B19' microstructure. Furthermore, the high phase transformation temperatures are consistent with a dominantly martensite microstructure,[34] indicating the absence of any significant driving force from the B2 fraction.

The elastic strain energy component, ΔH_{EL}, of the phase transformation enthalpy is necessary to accommodate transformational shape and volume changes. Increased Ni content increases density, which causes decreased elastic strain energy.[49,51] The strong negative correlation between enthalpy and RD (Figure 11) and the strong positive correlation between Ni content and RD discussed above (Figure 8) indicate that variation in Ni content is likely to significantly cause the observed variation in enthalpy within each trial. Furthermore, these correlations indicate that the lower average Ni content of batch $Ni_{(ii)}+Ti_{(ii)}$ relative to $Ni_{(i)}+Ti_{(i)}$ is likely to be a significant reason for the former's higher average enthalpy.

The frictional energy component, ΔH_{FR}, of the phase transformation enthalpy, represents energy dissipated to overcome frictional barriers during heating or cooling, and is a measure of the hysteresis, which can be measured from the DSC transformation temperature data as A_f–M_s.[50] The difference in hysteresis between the two batches is relatively small (Table 1 and Figure 9C), with a value of 29.5°C for $Ni_{(i)}+Ti_{(i)}$ and a value of 32.6°C for $Ni_{(ii)}+Ti_{(ii)}$, indicating that frictional losses may be marginally greater for $Ni_{(ii)}+Ti_{(ii)}$.

In summary, the recorded variation in phase transformation enthalpy can be primarily attributed to the chemical driving force from NiTi existing as B19' at room temperature, and variations in elastic strain energy negatively correlated with RD and Ni content. While the austenite phase transformation has to occur when the martensitic phase transformation occurs, the martensitic phase transformation is regarded as more important for contributing to the enthalpy response than the austenitic phase transformation (Figure 13). The variation in frictional driving force, measured by thermal hysteresis variation, is not significant.

Another noteworthy difference in the DSC curves of the two powder batches is the width of the heating transformation enthalpy curve A_f–A_s (Table 1). The average A_f–A_s was 20.5°C for $Ni_{(i)}+Ti_{(i)}$ and 32.6°C for $Ni_{(ii)}+Ti_{(ii)}$. This indicates the likelihood of higher chemical inhomogeneity in $Ni_{(ii)}+Ti_{(ii)}$ relative to $Ni_{(i)}+Ti_{(i)}$,[52,53] and is consistent with the higher variation in Ni content and RD that were measured in $Ni_{(ii)}+Ti_{(ii)}$ relative to $Ni_{(i)}+Ti_{(i)}$ (Figures 6 and 7B).

The low variation in martensitic start temperature across all tested specimens indicates low average overall Ni content. It is well known that at Ni contents below 50%at., martensitic start temperatures vary negligibly.[34,54] Average Ni content across the specimens, as measured by EDX mapping, was 49.4%. Although regions of coarse columnar with Ni content as high as 51.6%at. were identified (Figure 14), it appears that such regions do not contribute to phase transformation, and are likely to be composed of high proportions of Ni-rich precipitates. This is supported by the relatively low average phase transformation enthalpies (3.4 J/g for batch $Ni_{(i)}+Ti_{(i)}$ and 9.9 J/g for $Ni_{(ii)}+Ti_{(ii)}$). Phase transformation enthalpies for LPBF nitinol from pre-alloyed powder have been reported by Kordizadeh *et al.*[55] as 16–20 J/g[55] and by Khanlari *et al.*[56] as 13.8–15.7 J/g.[56] Analysis of the composition, size, and distribution of precipitates, as well as their effect on phase change and enthalpies, is beyond the scope of this work and is a recommended area for future research.

4.3. Microstructure

The multi-modal grain patterns throughout the microstructure (Figure 14) are evidence of a wide variation in the driving forces for grain nucleation and growth. Increased chemical inhomogeneity promotes increased constitutional supercooling and increases the complexity of phase transformation paths.[57] Higher non-uniform thermal distribution in the melt pool leads to a larger surface tension gradient, creating the conditions for increased Marangoni flow relative to pre-alloyed powders.[21] Furthermore, the highly localized nature of the Ni-Ti exothermic reactions

within the rapid cooling environment is expected to cause increased variation in thermal gradients.[16] The combined effect of these driving forces results in a greater grain size and morphology variety.

In summary, this study has established new insights into powder segregation during *in situ* alloying within the LPBF process and has found a direct link between powder segregation during deposition and nitinol phase transformation properties. The insights gained from this work into the effect of particle size and build distribution on properties will assist future studies in achieving improved microstructural and chemical homogeneity of *in situ* alloyed nitinol with tailored thermo-mechanical performance.

5. Conclusion

Powder segregation patterns of Ni and Ti powders in the LPBF process had a significant impact on RD and elasto-caloric properties of *in situ* alloyed nitinol, with regions of lower RD correlated with lower Ni content and higher phase transformation enthalpies compared to regions with higher Ni content. Powder segregation patterns between Ti and Ni particles varied more for an elementally blended batch with a d_{10}-d_{50}-d_{90} PSD of 33–47–65 μm than 21–32–48 μm.

The location and relative area fractions of unmelted and melted powder, as determined by the build layout, significantly impacted powder segregation patterns. It was found that powder segregation rates between Ti and Ni particles were higher for rougher substrates containing higher amounts of unmelted powder than smoother substrates containing higher amounts of melted and solidified powder. Furthermore, the position of the unmelted powder relative to the deposition arm sweep impacted powder segregation patterns throughout the build plate.

In addition to PSD and build layout, powder segregation patterns in the LPBF deposition bed were also affected by differences in material density between Ni and Ti and interparticle cohesive forces. The findings of this work concerning powder segregation within the LPBF process have significant implications for *in situ* alloying of nitinol and other alloys and can assist future studies in improving microstructural and chemical homogeneity and tailoring thermo-mechanical performance.

Acknowledgments

XRD testing was conducted at the Bernal Institute, University of Limerick, Limerick, Ireland. Micro-CT scanning was performed at the South-Eastern Applied Materials Research Centre, Waterford Institute of Technology, Waterford, Ireland. Optical microscopy and PSD measurements were conducted at the Nano Research Facility in Dublin City University.

Funding

This publication has emanated from research supported by a research grant from the Science Foundation Ireland (SFI) under grant number 16/RC/3872 and is co-funded by I-Form industry partner Fort Wayne Metals Ireland.

Conflict of interest

The authors declare that they have no competing interests.

Author contributions

Conceptualization: Declan Bourke, Dermot Brabazon
Formal analysis: Declan Bourke, Medad Monu, Inam Ul Ahad, Dermot Brabazon
Investigation: Declan Bourke, Medad Monu, Alexander Sloane, Inam Ul Ahad, Dermot Brabazon
Methodology: Declan Bourke, Medad Monu, Paul Healy, Alexander Sloane, Dermot Brabazon
Writing–original draft: Declan Bourke
Writing–review & editing: Inam Ul Ahad, Dermot Brabazon

Ethics approval and consent to participate

Not applicable.

Consent for publication

Not applicable.

Availability of data

Requests to access the datasets should be directed to the corresponding author.

References

1. Khoo ZX, Liu Y, An J, Chua CK, Shen YF, Kuo CN. A review of selective laser melted NiTi shape memory alloy. *Materials*. 2018;11(4):519.

   doi: 10.3390/ma11040519

2. Sharma N, Jangra KK, Raj T. Fabrication of NiTi alloy: A review. *Proc Inst Mech Eng Part J Mater Des Appl.* 2018;232(3):250-269.

   doi: 10.1177/1464420715622494

3. Farber E, Zhu JN, Popovich A, Popovich V. A review of NiTi shape memory alloy as a smart material produced by additive manufacturing. *Mater Today Proc.* 2020;30:761-767.

   doi: 10.1016/j.matpr.2020.01.563

4. Zhan J, Wu J, Ma R, Li K, Lin J, Murr LE. Tuning the functional properties by laser powder bed fusion with

partitioned repetitive laser scanning: Toward editable 4D printing of NiTi alloys. *J Manuf Process.* 2023;101:1468-1481.

doi: 10.1016/j.jmapro.2023.07.009

5. Duda T, Raghavan LV. 3D metal printing technology. *IFAC Pap.* 2016;49(29):103-110.

doi: 10.1016/j.ifacol.2016.11.111

6. Bormann T, Müller B, Schinhammer M, Kessler A, Thalmann P, De Wild M. Microstructure of selective laser melted nickel-titanium. *Mater Charact.* 2014;94:189-202.

doi: 10.1016/j.matchar.2014.05.017

7. Chekotu JC, Groarke R, O'Toole K, Brabazon D. Advances in selective laser melting of nitinol shape memory alloy part production. *Materials (Basel).* 2019;12(5):809.

doi: 10.3390/ma12050809

8. Alagha AN, Hussain S, Zaki W. Additive manufacturing of shape memory alloys: A review with emphasis on powder bed systems. *Mater Des.* 2021;204:109654.

doi: 10.1016/j.matdes.2021.109654

9. Elahinia M, Shayesteh Moghaddam N, Taheri Andani M, Amerinatanzi A, Bimber BA, Hamilton RF. Fabrication of NiTi through additive manufacturing: A review. *Prog Mater Sci.* 2016;83:630-663.

doi: 10.1016/j.pmatsci.2016.08.001

10. Bourke D, Selvam KT, Obeidi MA, Ul Ahad I, Brabazon D. Effect of powder and process parameters on *in-situ* alloying of nitinol during laser powder bed fusion. *J Mater Res Technol.* 2024;30:7988-7997.

doi: 10.1016/j.jmrt.2024.05.178

11. Wang S, Shi Y, Fan K, Wang Q, Li Y, Teng X. Microstructure and elastocaloric effect of NiTi shape memory alloy *in-situ* synthesized by laser directed energy deposition additive manufacturing. *Mater Charact.* 2024;210:113831.

doi: 10.1016/j.matchar.2024.113831

12. Ewald S, Kies F, Hermsen S, Voshage M, Haase C, Schleifenbaum JH. Rapid alloy development of extremely high-alloyed metals using powder blends in laser powder bed fusion. *Materials(Basel).* 2019;12(10):1706.

doi: 10.3390/ma12101706

13. Wang C, Tan XP, Du Z, *et al.* Additive manufacturing of NiTi shape memory alloys using pre-mixed powders. *J Mater Process Technol.* 2019;271:152-161.

doi: 10.1016/j.jmatprotec.2019.03.025.

14. Zhang B, Chen J, Coddet C. Microstructure and transformation behavior of *in-situ* shape memory alloys by selective laser melting Ti-Ni mixed powder. *J Mater Sci Technol.* 2013;29(9):863-867.

doi: 10.1016/j.jmst.2013.05.006

15. Stoll P, Spierings A, Wegener K. SLM processing of elementally blended NiTi shape memory alloy. *Procedia CIRP.* 2020;95:121-126.

doi: 10.1016/j.procir.2020.02.250

16. Mosallanejad MH, Niroumand B, Aversa A, Saboori A. *In-situ* alloying in laser-based additive manufacturing processes: A critical review. *J Alloys Compd.* 2021;872:159567.

doi: 10.1016/j.jallcom.2021.159567

17. Li H, Brodie EG, Hutchinson C. Predicting the chemical homogeneity in laser powder bed fusion (LPBF) of mixed powders after remelting. *Addit Manuf.* 2023;65:103447.

doi: 10.1016/j.addma.2023.103447

18. Shoji Aota L, Bajaj P, Zschommler Sandim HR, Aimé Jägle E. Laser powder-bed fusion as an alloy development tool: Parameter selection for *in-situ* alloying using elemental powders. *Materials.* 2020;13(18):3922.

doi: 10.3390/ma13183922

19. Knieps MS, Reynolds WJ, Dejaune J, Clare AT, Evirgen A. *In-situ* alloying in powder bed fusion: The role of powder morphology. *Mater Sci Eng A.* 2021;807:140849.

doi: 10.1016/j.msea.2021.140849

20. Mussatto A, Groarke R, O'Neill A, Obeidi MA, Delaure Y, Brabazon D. Influences of powder morphology and spreading parameters on the powder bed topography uniformity in powder bed fusion metal additive manufacturing. *Addit Manuf.* 2021;38:101807.

doi: 10.1016/j.addma.2020.101807

21. Zhao C, Fezzaa K, Cunningham RW, *et al.* Real-time monitoring of laser powder bed fusion process using high-speed X-ray imaging and diffraction. *Sci Rep.* 2017;7:3602.

doi: 10.1038/s41598-017-03761-2

22. Thiedemann U, Rösner-Kuhn M, Drewes K, Kuppermann G, Frohberg MG. Temperature dependence of the mixing enthalpy of liquid Ti-Ni and Fe-Ti-Ni alloys. *J Non Cryst Solids.* 1999;250-253:329-335.

doi: 10.1016/S0022-3093(99)00258-6

23. Chen Y, Zhang X, Parvez MM, Liou F. A review on metallic alloys fabrication using elemental powder blends by laser powder directed energy deposition process. *Materials (Basel).* 2020;13(16):3562.

doi: 10.3390/ma13163562

24. Chmielewska A, Wysocki B, Buhagiar JP, *et al. In situ* alloying of NiTi: Influence of laser powder bed fusion (LBPF) scanning strategy on chemical composition. *Mater Today Commun.* 2022;30:103007.

doi: 10.1016/j.mtcomm.2021.103007

25. Yadroitsev I. *Selective Laser Melting: Direct Manufacturing of 3D-Objects by Selective Laser Melting of Metal Powders.*

Germany: LAP Lambert Academic Publishing; 2009.

26. Aboulkhair NT, Everitt NM, Ashcroft I, Tuck C. Reducing porosity in AlSi10Mg parts processed by selective laser melting. *Addit Manuf.* 2014;1-4:77-86.

    doi: 10.1016/j.addma.2014.08.001

27. Zhao C, Liang H, Luo S, Yang J, Wang Z. The effect of energy input on reaction, phase transition and shape memory effect of NiTi alloy by selective laser melting. *J Alloys Compd.* 2020;817:153288.

    doi: 10.1016/j.jallcom.2019.153288

28. Chmielewska A, Wysocki BA, Gadalińska E, *et al.* Laser powder bed fusion (LPBF) of NiTi alloy using elemental powders: The influence of remelting on printability and microstructure. *Rapid Prototy J.* 2022;28:1845-1868.

    doi: 10.1108/RPJ-08-2021-0216

29. Nan W, Pasha M, Bonakdar T, *et al.* Jamming during particle spreading in additive manufacturing. *Powder Technol.* 2018;338:253-262.

    doi: 10.1016/j.powtec.2018.07.030

30. Ahmed M, Pasha M, Nan W, Ghadiri M. A simple method for assessing powder spreadability for additive manufacturing. *Powder Technol.* 2020;367:671-679.

    doi: 10.1016/j.powtec.2020.04.033

31. Xu R, Nan W. Analysis of the metrics and mechanism of powder spreadability in powder-based additive manufacturing. *Addit Manuf.* 2023;71:103596.

    doi: 10.1016/j.addma.2023.103596

32. He Y, Hassanpour A, Bayly AE. Combined effect of particle size and surface cohesiveness on powder spreadability for additive manufacturing. *Powder Technol.* 2021;392:191-203.

    doi: 10.1016/j.powtec.2021.06.046

33. Giraud M, Gatumel C, Vaudez S, *et al.* Investigation of a granular Bond number based rheological model for polydispersed particulate systems. *Chem Eng Sci.* 2020;228:115971.

    doi: 10.1016/j.ces.2020.115971

34. Frenzel J, George EP, Dlouhý A, Somsen C, Wagner WF, Eggeler G. Influence of Ni on martensitic phase transformations in NiTi shape memory alloys. *Acta Mater.* 2010;58(9):3444-3458.

    doi: 10.1016/j.actamat.2010.02.019

35. Groarke R, Vijayaraghavan RK, Powell D, Rennie A, Brabazon D. Powder characterization-methods, standards, and state of the art. In: Yadroitsev I, Yadroitsava I, Du Plessis A, MacDonald E, editors. *Fundamentals of Laser Powder Bed Fusion of Metals. In Additive Manufacturing Materials and Technologies*. Netherlands: Elsevier; 2021. p. 491-527.

    doi: 10.1016/B978-0-12-824090-8.00006-8

36. Tondare VN, Whiting JG, Pintar AL, Moylan S, Neveu A, Francqui F. An interlaboratory study for assessing repeatability and reproducibility of the data generated by rotating drum powder rheometers (part 1: Granudrum). *Powder Technol.* 2024;441:119810.

    doi: 10.1016/j.powtec.2024.119810

37. Neveu A, Francqui F, Lumay G. Measuring powder flow properties in a rotating drum. *Measurement*. 2022;200:111548.

    doi: 10.1016/j.measurement.2022.111548

38. ISO. *ISO/ASTM TR 52952:2023*. ISO. Available from: https://www.iso.org/standard/83717.html [Last accessed on 2025 Apr 03].

39. *Crystallography Open Database*. Available from: https://www.crystallography.net/cod/index.php [Last accessed on 2024 Feb 06].

40. Rodriguez-Carvajal J. Introduction to the program FULLPROF: Refinement of crystal and magnetic structures from powder and single crystal data, Laboratoire Léon Brillouin (CEA-CNRS). France: CEA/Saclay; 2001. [Online]. Available: https://www.researchgate.net/publication/267375610

41. *Match! - Phase Analysis using Powder Diffraction*. Available from: https://www.crystalimpact.de/match [Last accessed on 2024 Nov 04].

42. Wang J, Zhu R, Liu Y, Zhang L. Understanding melt pool characteristics in laser powder bed fusion: An overview of single- and multi-track melt pools for process optimization. *Adv Powder Mater.* 2023;2(4):100137.

    doi: 10.1016/j.apmate.2023.100137

43. Capozzi LC, Sivo A, Bassini E. Powder spreading and spreadability in the additive manufacturing of metallic materials: A critical review. *J Mater Process Technol.* 2022;308:117706.

    doi: 10.1016/j.jmatprotec.2022.117706

44. *ASM Material Data Sheet*. Available from: https://asm.matweb.com/search/specificmaterial.asp?bassnum=ntime35a [Last accessed on 2025 Apr 11].

45. *Nickel, Cobalt, and their Alloys (asm Specialty Handbook) [PDF] [12ncqllkk93o]*. Available from: https://vdoc.pub/documents/nickel/cobalt/and/their/alloys/asm/specialty/handbook/12ncqllkk93o [Last accessed on 2025 Apr 11].

46. Yadroitsev I, Krakhmalev P, Yadroitsava I. Titanium alloys manufactured by *in situ* alloying during laser powder bed fusion. *JOM*. 2017;69(12):2725-2730.

    doi: 10.1007/s11837-017-2600-7

47. Spierings A, Levy G. *Comparison of Density of Stainless Steel 316 L Parts Produced with Selective Laser Melting using Different Powder Grades*; 2009. Available from: https://www.semanticscholar.org/paper/comparison/

of/density/of/stainless/steel/316/l/with/spierings/levy/e5a132bae55615a773d2468c4692c28865abf313 [Last accessed on 2025 Feb 26].

48. Snow Z, Martukanitz R, Joshi S. On the development of powder spreadability metrics and feedstock requirements for powder bed fusion additive manufacturing. *Addit Manuf.* 2019;28:78-86.

doi: 10.1016/j.addma.2019.04.017

49. Ortín J, Planes A. Thermodynamic analysis of thermal measurements in thermoelastic martensitic transformations. *Acta Metall.* 1988;36(8):1873-1889.

doi: 10.1016/0001-6160(88)90291-X

50. Humbeeck JV, Stalmans R, Chandrasekaran M, Delaey L. *On the Stability of Shape Memory Alloys*. Netherlands: Elsevier; 1990. p. 96-105.

doi: 10.1016/B978-0-7506-1009-4.50012-3

51. Khalil-Allafi J, Amin-Ahmadi B. The effect of chemical composition on enthalpy and entropy changes of martensitic transformations in binary NiTi shape memory alloys. *J Alloys Compd.* 2009;487(1):363-366.

doi: 10.1016/j.jallcom.2009.07.135

52. Sam J, Franco B, Ma J, Karaman I, Elwany A, Mabe JH. Tensile actuation response of additively manufactured nickel-titanium shape memory alloys. *Scr Mater.* 2018;146:164-168.

doi: 10.1016/j.scriptamat.2017.11.013

53. Zhang Q, Hao S, Liu Y, *et al.* The microstructure of a selective laser melting (SLM)-fabricated NiTi shape memory alloy with superior tensile property and shape memory recoverability. *Appl Mater Today*. 2020;19:100547.

doi: 10.1016/j.apmt.2019.100547

54. Wang X, Yu J, Liu J, *et al.* Effect of process parameters on the phase transformation behavior and tensile properties of NiTi shape memory alloys fabricated by selective laser melting. *Addit Manuf.* 2020;36:101545.

doi: 10.1016/j.addma.2020.101545

55. Kordizadeh F, Mohajerani S, Safaei K, *et al.* Investigating the elastocaloric effect of the NiTi fabricated by laser powder bed fusion: Effect of the building orientation. *Materialia*. 2023;30:101817.

doi: 10.1016/j.mtla.2023.101817

56. Khanlari K, Shi Q, Li K, Hu K, Cao P, Liu X. Effects of printing volumetric energy densities and post-processing treatments on the microstructural properties, phase transformation temperatures and hardness of near-equiatomic NiTinol parts fabricated by a laser powder bed fusion technique. *Intermetallics*. 2021;131:107088.

doi: 10.1016/j.intermet.2021.107088

57. Collins C, Brice DA, Samimi P, Ghamarian I, Fraser HL. Microstructural control of additively manufactured metallic materials. *Annu Rev Mater Res.* 2016;46:63-91.

doi: 10.1146/annurev-matsci-070115-031816